Application of the Variational Mode Decomposition (VMD) method to river tides

Min Gan[1,2,3], Haidong Pan[4,5,6,7*], Yongping Chen[1,2], Shunqi Pan[3]

[1]State Key Laboratory of Hydrology-Water Resources & Hydraulic Engineering, Nanjing 210098, China

[2]College of Harbor, Coastal, and Offshore Engineering, Hohai University, Nanjing 210098, China

[3]Hydro-environmental Research Centre, School of Engineering, Cardiff University, Cardiff CF24 3AA, United Kingdom

[4]First Institute of Oceanography, and Key Laboratory of Marine Science and Numerical Modeling, Ministry of Natural Resources, Qingdao 266061, China

[5]Laboratory for Regional Oceanography and Numerical Modeling, Pilot National Laboratory for Marine Science and Technology, Qingdao 266237, China

[6]Shandong Key Laboratory of Marine Science and Numerical Modeling, Qingdao 266061, China

[7]Key Laboratory of Physical Oceanography, Ocean University of China, Qingdao 266003, China

Corresponding Author:

Haidong Pan (panhaidong@fio.org.cn; panhaidong_phd@qq.com)

ABSTRACT

Tides in fluvial estuaries are distorted by non-stationary river discharge, which makes the analysis of estuarine water levels less accurate when using the conventional tidal analysis method. As a powerful and widely-used method for non-stationary and nonlinear time series, the application of Variational Mode Decomposition (VMD) method to non-stationary tides is nonexistent. This paper aims to illustrate and verify the suitability of the VMD method as a new tidal analysis tool for river tides. The efficiency of VMD is validated by the measurements from the Columbia River Estuary. VMD strictly divides different tidal species into different modes, and thus avoids mode mixing. Compared to VMD, Ensemble Empirical Mode Decomposition (EEMD), which is another commonly-used method, fails to completely solve the problem of mode mixing. The observed water levels at Longview station are decomposed into 12 modes via VMD. Based on the mean periods and amplitudes of each VMD mode, the 12 VMD modes sequentially correspond to the tidal species from the sub-tides (D_0), diurnal tides (D_1), semi-diurnal tides (D_2), and up to D_{11} tides. The non-stationary characteristics of tides influenced by river discharge are accurately captured by VMD without mode mixing. The results also show that the EEMD and VMD modes can capture the subtidal signals better than the nonstationary tidal harmonic analysis tool (NS_TIDE). As a general method, the VMD mode can also be used for other research purposes related to non-stationary tides, such as detiding.

Keywords: VMD; EEMD; NS_TIDE; river tides; tide-river interplay

1. Introduction

Tides are the periodic rise and fall of sea levels induced by the combined effects of the gravitational forces of the Moon and the Sun acting on the orbiting and rotating Earth (Amin, 1982). Tidal fluctuations including vertical and horizontal tides are the basic movements of sea water. They are very important to human activities in the deep sea and coastal areas such as navigation, energy utilization, oceanographic engineering and aquaculture (Pan et al., 2017). The most widely used approach in tidal data analysis is the Classical Harmonic Analysis (CHA), which assumes water levels can be represented by a linear combination of sinusoidal terms (Foreman and Henry, 1989; Pan et al., 2018b). These sinusoidal terms called tidal constituents are perfectly stationary in the CHA. Namely, the amplitudes and phases of tidal constituents are assumed constant. In most tidal observations, this stationary assumption is reasonable. Thus, CHA has an excellent performance in explaining observed water levels (usually over 90 percent of the variance) (Hoitink and Jay, 2016).

Tidal phenomena, such as internal tides, tides in tidal rivers and ice-covered bay are highly non-stationary. For these tidal processes, the stationary assumption of CHA is unsuitable. In such conditions, CHA performs badly in hindcasting and forecasting water levels and only provides time-averaged values of time-varying tidal properties (Jay and Flinchem, 1997; Pan et al., 2018a). To obtain the time-dependent tidal amplitudes and phases, CHA can be conducted by adding a time window (Jay and Flinchem, 1997; Guo et al., 2015), which becomes the short-term harmonic analysis

(STHA). Although the STHA method can extract the time-dependent tidal properties, it can only separate a limited number of the main tidal constituents. Moreover, STHA may provide inaccurate results when the variation of river discharge is strong (Jalón-Rojas et al., 2018).

To acquire insights into underlying dynamics of highly non-stationary tidal signals, Kukulka and Jay (2003a) proposed a framework in describing the decay of tides along the estuary with the consideration of upstream river discharge. They also derived a theory in modelling the sub-tidal water levels in their following work (Kukulka and Jay 2003b). Accordingly, Matte et al. (2013, 2014) developed the non-stationary harmonic analysis tool (NS_TIDE) by directly embedding the frameworks of Kukulka and Jay (2003a, b) into the CHA basis functions. Subsequently, Pan et al. (2018b) developed a new version of NS_TIDE in which the contribution from coastal upwelling and downwelling can be considered. NS_TIDE has been widely used to study the river-tide dynamics in the fluvial estuaries, such as the Columbia River estuary (Matte et al., 2013; Pan et al., 2018a, b; Gan et al., 2021), Yangtze River estuary (Gan et al., 2019; Chen et al., 2020), St. Lawrence River estuary (Matte et al., 2014, 2018, 2019), and Pearl River Delta (Cai et al., 2018; Zhang et al., 2018). Although NS_TIDE performs much better than CHA in tidal rivers, it also has some limitations. First, synchronous river discharge observations relative to water levels are needed to perform non-stationary harmonic analysis using NS_TIDE. Second, based on the theoretical tide-river interaction model, NS_TIDE cannot be applied to non-stationary tidal processes with other dynamic mechanisms, *i.e.*, internal tides (Pan et al., 2018a, b).

Signal analysis tools, such as the Continuous Wavelet Transform (CWT) and Complex Demodulation methods, are good supplements to study the non-stationary tidal signals. Jay and Flinchem (1999) compared the model performance of the CWT, STHA, and the modified STHA (mSTHA) methods. Their results show that the CWT model can provide better results than the STHA and mSTHA methods once the time window's length is longer than a few days. A system introduction about the application of the CWT method in river tides is given in the study of Flinchem and Jay (2000). Relative to the CWT method, the Complex Demodulation is more suitable to determine the time variations of tidal signals in a particular frequency band (Jay and Kukulka, 2003). For instance, Jalón-Rojas et al. (2018) applied the Complex Demodulation method to extract the time-dependent amplitudes and phase of semi-diurnal (D2) and quarter-diurnal (D4) tides of the Gironde Estuary.

As a powerful and widely-used method for non-stationary and nonlinear time series, Empirical Mode Decomposition (EMD, Huang et al., 1998) is another signal analysis tool that has been widely used to analyze non-stationary tides in recent years (Cheng et al., 2017; Devlin et al., 2020). Pan et al. (2018a, b) first applied the EMD method to analyze river tides. EMD obtained the non-stationary characteristics of diurnal and semi-diurnal tides related to river discharge successfully. By comparing the results of NS_TIDE and EMD, it is found that the error in NS_TIDE hindcast mainly comes from the less accurate sub-tidal water levels inversed by NS_TIDE (Pan et al., 2018b). Though powerful, the EMD method is disturbed by a serious "mode mixing" problem, which is defined as either a single mode of the EMD method including widely disparate signals, or a similar signal residing in different modes of the EMD model (Zhang et al., 2010). In terms of tidal levels, the mode mixing can be reflected in that the energy of the same tidal species (a group of tidal constituents with similar frequencies (Hoitink and Jay, 2016)) exist in more than one EMD mode. Therefore, the EMD modes may need to be combined within a window of frequency to connect the EMD modes to the physical processes (Ezer, 2019).

To solve this mode mixing problem, Wu and Huang (2009) proposed a noise-assisted EMD method, namely Ensemble EMD (EEMD). Devlin et al. (2020) used the EEMD method to analyze multi-timescale tidal variability in the Indian Ocean. However, the mode mixing phenomenon still exists in the results of EEMD when dealing with river tides (details displayed in section 4). Variational Mode Decomposition (VMD), recently proposed by Dragomiretskiy and Zosso (2014), is an alternative method to EMD. VMD is a generalization of the classic Wiener filter into multiple, adaptive bands (Dragomiretskiy and Zosso, 2014). The VMD method obtains each mode from the frequency domain, which enables the VMD model to be less sensitive to noises and has the advantage of avoiding mode mixing. Therefore, the VMD method has been widely applied to analyze the neuromuscular signal, audio signal, and climate data (Zosso, 2021).

The main objective of this research is to apply the VMD method to the river tides of the Columbia River Estuary where the river-tide interaction plays a dominant influence on the water levels of tidal reaches. As the influence of seasonal wind on the water levels of the Columbia River Estuary is insignificant (Jay et al., 2014), it is ignored in this study. River tides are selected because they are the simplest non-stationary tidal phenomenon and the only one for which both abundant observations and detailed theoretical models exist (Jay and Flinchem, 1997, 1999). The results of the VMD modes are further compared with the results of the NS_TIDE and EEMD models to fully compare their advantages and disadvantages. Moreover, the application of the VMD model in other physical processess related to river tides is also investigated.

This paper is structured as follows. The NS_TIDE, EEMD and VMD methods are described in section 2. The study area and data are shown in section 3. The results of NS_TIDE, EEMD and VMD are displayed and discussed in section 4 and section 5, respectively. Conclusions are presented in section 6.

2. Methodology

2.1 Non-stationary Harmonic Analysis Model (NS_TIDE)

In the CHA model, observed water levels can be expressed as (Pawlowicz et al., 2002):

$$H(t) = Z + \sum_{i=1}^{N} (a_i cos\sigma_i + b_i sin\sigma_i) \quad (1)$$

where $H(t)$ is the observed estuarine water level at time t; Z is the mean water level

(MWL); i is the index of tidal constituents and N is the total number of tidal constituents to be resolved; σ_i is the frequency of the i^{th} tidal constituent.

In the NS_TIDE model, time-invariant Z, a_i and b_i in **Eq. (1)** are replaced by the nonlinear functions of time-changing river discharge Q and greater diurnal tidal range R in the semi-diurnal tidal regime of a reference station near the estuary mouth:

$$H(t) = Z(Q,R) + \sum_{i=1}^{N} (a_i(Q,R)cos\sigma_i + b_i(Q,R)sin\sigma_i) \tag{2}$$

$$Z(Q,R) = c_0 + c_1 Q^{p_z} + c_2 \frac{R^{q_z}}{Q^{r_z}} \tag{3}$$

$$a_i(Q,R) = d_0 + d_1 Q^{p_f} + d_2 \frac{R^{q_f}}{Q^{r_f}} \tag{4}$$

$$b_i(Q,R) = e_0 + e_1 Q^{p_f} + e_2 \frac{R^{q_f}}{Q^{r_f}} \tag{5}$$

where (p_z, q_z, r_z) and (p_f, q_f, r_f) are the unknown exponents to be iteratively determined; c_h, d_h, and e_h $(h = [0,2])$ are the unknown coefficients to be solved. The first and second terms on the right-hand sided of **Eq. (2)** are respectively the "stage" and the "tidal-fluvial" models in NS_TIDE, which are adapted from the works of Kukulka and Jay (2003a, b). The stage model describes the sub-tidal water levels (oscillations with periods obviously greater than 1 day), while the "tidal-fluvial" model explains the diurnal, semi-diurnal and higher frequency tidal constituents. $d_1 Q^{p_f} (e_1 Q^{p_f})$ is the river discharge term representing the nonlinear decay effect of river discharge on tides. The coefficient $d_1(e_1)$ is often negative, indicating tidal amplitudes decrease when the river discharge increases. $\frac{R^{q_f}}{Q^{r_f}}$ is the tidal range term which represents the nonlinear tidal-river interplay induced by neap-spring variability.

When river discharge is large, the changes of tidal properties induced by the tidal range term become less important. With Q, R and $H(t)$ known, **Eq. (2)** can be solved using a least squares fitting method. In the NS_TIDE model, the iteratively reweighted least squares (IRLS) is used to improve the overall fitting (Leffler and Jay, 2009).

2.2 Ensemble Empirical Mode Decomposition (EEMD)

The EMD method is developed by Huang et al. (1998). As an adaptive and recursive signal decomposition algorithm designed for nonlinear and non-stationary signals, EMD is widely used to analyze numerous kinds of geophysical data, such as sea levels (Ezer, 2013; Cheng et al., 2016; Ezer et al., 2016), sea surface temperature (Wu et al., 2008) and land surface air temperature (Ji et al., 2014). Via the EMD method, a complicated non-stationary time series can be decomposed into a finite number of components, which are usually called intrinsic mode functions (IMFs). Those IMFs are not restricted to a narrow band signal, and their amplitudes, phases and frequencies are all time-variant. A time series of water level observations can be decomposed using the EMD method in the following form:

$$H(t) = \sum_{m=1}^{M} c_m(t) + r(t) \tag{6}$$

where m is the index of IMFs; M is the total number of IMFs which contain periodic signals; $c_m(t)$ is the m^{th} IMF; $r(t)$ is the last IMF representing the trend term of the observations. In total, there are $M+1$ IMFs, which are related to the factors such as the variation of the observations, the length of the record, as well as the stoppage criteria of the sifting process (Pan et al., 2018a). The trend term $r(t)$ obtained by the EMD method is often monotonic. Therefore, it does not contain any oscillation of a fixed period.

The main processes of the EEMD method are described as follows (Wu et al., 2008):

Step 1: Generate a white noise series and add it to the targeted signal. Decompose the noise-added signal into a specified number of IMFs via the EMD method.

Step 2: Repeat step 1 a specified number of times. Note that the added white noise series are distinct each time.

Step 3: Average the corresponding IMFs as the final results of EEMD.

The effects of the EEMD decomposition are that the added white noise time series cancel each other once they are summed up. The mean IMFs of EEMD preserve the good properties of the EMD method, while the strength of mode mixing in EEMD obviously decreases relative to the EMD model (Wu et al., 2008).

2.3 Variational Mode Decomposition (VMD)

The VMD method generally treats the problem of mode decomposition as an optimization problem by decomposing 1-dimensional input signal into a specified number of modes. The signal gets fully reproduced by summing up the K number of decomposition modes

$$H(t) = \sum_{k=1}^{K} u_k(t) \tag{7}$$

where k is the index of modes; K is the total number of modes; $u_k(t)$ is the k^{th} mode and it is an amplitude-modulated-requency-modulated signal, which can be expressed as:

$$u_k(t) = A_k(t)cos\big(\varphi_k(t)\big) \tag{8}$$

where $A_k(t)$ and $\varphi_k(t)$ are the time-dependent envelope and the phase of the k^{th} mode, respectively. The related instantaneous frequency $\omega_k(t)$ of the k^{th} mode is assumed to vary slowly relative to the phase and is nonnegative. It can be calculated as:

$$\omega_k(t) = \frac{\partial \varphi_k(t)}{\partial t} \tag{9}$$

The decomposition process of the time series by the VMD method can be expressed as a constrained variational problem (Dragomiretskiy and Zosso, 2014) whose objective function is:

$$\begin{aligned} &\min_{\{u_k\}\{\bar{\omega}_k\}} \left\{ \sum_{k=1}^{K} \left\| \partial_t \left[\left(\delta(t) + \frac{j}{\pi t} \right) * u_k(t) \right] e^{-j\bar{\omega}_k t} \right\|_2^2 \right\} \\ &s.t. \sum_{k=1}^{K} u_k(t) = H(t) \end{aligned} \tag{10}$$

where $\{u_k\} = \{u_1, \dots, u_K\}$ and $\{\overline{\omega}_k\} = \{\overline{\omega}_1, \dots, \overline{\omega}_K\}$ are the sets of all modes and their related center frequencies; $\delta(t)$ is the Dirac function; * represents the convolution; $j = \sqrt{-1}$.

Dragomiretskiy and Zosso (2014) used a quadratic penalty term and Lagrangian multiplier to transform **Eq. (10)** to an unconstrained optimization problem:

$$L\left(\{u_k\},\{\bar{\omega}_k\},\lambda\right)=\alpha\sum_{k=1}^{K}\left\|\partial_t\left[\left(\delta(t)+\frac{j}{\pi t}\right)*u_k(t)\right]e^{-j\bar{\omega}_k t}\right\|_2^2+\left\|H(t)-\sum_{k=1}^{K}u_k(t)\right\|_2^2+\left\langle\lambda(t),H(t)-\sum_{k=1}^{K}u_k(t)\right\rangle \tag{11}$$

where α is the regularization parameter representing the variance of the white noise; $\lambda(t)$ is the Lagrangian multiplier.

The solution of **Eq. (11)** is by using the alternate direction method of multipliers (ADMM) method. Only the final expressions of the ADMM method are summarized in this study. For more details, the reader can refer to Dragomiretskiy and Zosso (2014). The solution of each mode in the frequency domain can be expressed as:

$$\hat{u}_k^{n+1}(\omega)=\frac{\hat{H}(\omega)-\sum_{i<k}\hat{u}_i^{n+1}(\omega)+\sum_{i>k}\hat{u}_i^{n}(\omega)+\dfrac{\hat{\lambda}^n(\omega)}{2}}{1-2\alpha\left(\omega-\bar{\omega}_k\right)} \tag{12}$$

where $\hat{u}_k(\omega)$, $\widehat{H}_k(\omega)$, and $\hat{\lambda}_k(\omega)$ denote the spectrum of $u_k(t)$, $H(t)$, and $\lambda(t)$, respectively; The superscript $n+1$ and n denote the results of the current and previous steps of the iteration process, respectively.

During each update of $\hat{u}_k^{n+1}(\omega)$, the corresponding center frequency $\bar{\omega}_k^{n+1}$ is subsequently updated as the center-of-gravity of the power spectrum of each mode:

$$\bar{\omega}_k^{n+1}=\frac{\int_0^\infty \omega\left|\hat{u}_k^{n+1}(\omega)\right|^2 d\omega}{\int_0^\infty \left|\hat{u}_k^{n+1}(\omega)\right|^2 d\omega} \tag{13}$$

Once all the $\hat{u}_k^{n+1}(\omega)$ and $\bar{\omega}_k^{n+1}$ are obtained, the $\hat{\lambda}_k^{n+1}(\omega)$ is updated as:

$$\hat{\lambda}_k^{n+1}(\omega)=\hat{\lambda}_k^{n}(\omega)+\tau\left(\hat{H}(\omega)-\sum_{k=1}^{K}\hat{u}_k^{n+1}(\omega)\right) \tag{14}$$

where τ is user-defined coefficient for dual ascent to enforce the exact signal reconstruction (Ni et al., 2018).

The convergence state of the model iteration process is defined as:

$$\sum_{k=1}^{K} \frac{\left\| \hat{u}_k^{n+1}(\omega) - \hat{u}_k^{n}(\omega) \right\|_2^2}{\left\| \hat{u}_k^{n}(\omega) \right\|_2^2} < \varepsilon \tag{15}$$

where ε is the user-defined coefficient for the judgement of model convergence. When the VMD modes in the frequency domain reach the convergence state, their results in the time domain can be obtained by the inverse of Fourier transform:

$$u_k(t) = R\left\{ ift\left(\hat{u}_k(\omega) \right) \right\} \tag{16}$$

where $R\{\}$ represents the real part; ift represents the inverse of Fourier transform.

2.4 Flowchart

A flowchart is given in **Fig. 1** for a better illustration of the roadmap of this research. The water level measurements at Longview station are analyzed by NS_TIDE, EEMD and VMD models, respectively. The NS_TIDE model is used to extract the time-dependent amplitudes and phases of tidal constituents to describe the influence of external force (river discharge) on tidal constituents. Moreover, the sub-tidal water levels (D0 tidal frequency band) modelled by the NS_TIDE model are compared with the sub-tidal water levels extracted from the EEMD and the VMD models. In comparison with the NS_TIDE model, the attention of the EEMD and VMD model results is on tidal species rather than specific tidal constituents. When the tidal signals in different tidal frequency bands, such as D1 and D2 tides, are filtered by the EEMD and VMD models, Fourier analysis is conducted on these tidal signals within different frequency band to compare whether there exists mode mixing in the results of the VMD model.

3. Study area and data

The Columbia River (**Fig. 2**) has a watershed of ~660500 km^2 and an annual average flow of ~7500 m^3/s (Jay and Flinchem, 1997). The Willamette River, which is the largest tributary of the Columbia River, enters the river main stem at Portland, ~160 river kilometer (rkm) from the ocean, with an annual average flow of ~950 m^3/s (Matte et al., 2013; Pan and Lv, 2019). As the third largest river in the United States, the Columbia River is important and essential for local fisheries industry, hydropower, ocean transport and other economic sectors. The tides in the Columbia River estuary (CRE) are diurnal (D_1) and semi-diurnal (D_2) mixed with a D_2/D_1 ratio of ~1.8 at the CRE mouth (Jay et al., 2011; Moftakhari et al., 2016; Pan et al., 2018a, b). The diurnal tidal range at Astoria (**Fig. 2**, rkm 29) varies from ~1.59 to 3.83 m. As tides propagate landward, tidal range gradually decreases and becomes nearly zero at Bonneville dam at rkm 234 (Jay et al., 2011; Jay et al., 2014). Hourly water level records (**Fig. 3a**) for a year period (January 2003 - December 2003) from Astoria (rkm 29) and Longview (rkm 107) stations (**Fig. 2**) provided by the National Oceanic and Atmospheric Administration (NOAA) are analyzed in this research. Additional river discharge data (**Fig. 3b**) for the Willamette River and the main stem of the Columbia River (at

Bonneville Dam) are provided by the U.S. Geological Survey (USGS).

The skewness coefficient referred to the work of Nidzieko (2011) is used to evaluate the tide characteristics of the CRE. The skewness coefficient of the time derivative of the tide levels at Astoria (29 rkm) is close to zero, indicating the symmetric tide. This means the tides at Astoria are nearly stationary and are only under an ignorable influence of upstream river discharge (**Fig. 3a**). At Astoria, the hindcast of CHA (Pawlowicz et al., 2002) explains 97.5% of the observed signal variance, with a root-mean-square error (RMSE) of 0.13 m and a maximum absolute error (MAE) of 0.61 m for tidal heights. The largest tidal constituent is M_2 tide, followed by K_1 tide with amplitudes of 0.94 and 0.44 m, respectively. The amplitudes of overtide and compound constituents (less than 0.04 m) are much smaller than those of major diurnal and semi-diurnal constituents.

The skewness coefficient of the time derivative of the tide levels at Longview station significantly increases to 0.83, indicating an asymmetric tide (Nidzieko, 2011). More specifically, the rising tide duration is shorter than the falling tide duration at Longview station. In comparison with Astoria, the tides at Longview station are significantly distorted and damped by river discharge (**Fig. 3a**). The CHA hindcast only explains 80.0% of the signal variance and has an RMSE of 0.24 m and an MAE of 1.80 m. This unsatisfactory result indicates that CHA is unable to describe the nonlinear process of tidal-fluvial interplay. The amplitudes of M_2 and K_1 tides at Longview decrease to 0.43 and 0.20 m, respectively. The amplitudes of shallow water constituents obtained from the CHA method have an obvious increase especially the Msf and M_4 tides (**Table 1**) due to the nonlinear interaction between tides and river discharge. Other high-frequency constituents such as the M_6 and M_8 tides are still very weak though their amplitudes have increased.

4. Results

4.1 The results of NS_TIDE

Astoria is selected as the reference station in the NS_TIDE model for providing the ocean tidal range forcing. The parameter η for the modified Rayleigh criterion (Matte et al., 2013) in NS_TIDE is set to 0.20 (see **Table 2**, 26 tidal constituents are resolved). It should be noted that the long-period tidal constituents, such as Mf (13.66 days), Msf (14.77 days), Mm (27.55 days), Ssa (182.59 days), and Sa (365.18 days) tides are indirectly contained in the variations of the sub-tidal water levels (**Eq. (3)**) and do not be extracted separately to avoid overfitting. The hindcast of the NS_TIDE model is performed with tidal constituents whose time-averaged signal-to-noise ratios (SNRs) larger than two.

Results obtained by NS_TIDE are obviously improved compared to CHA at Longview: the NS_TIDE hindcast explains 94.48% of the signal variance and has an RMSE of 0.13 m and an MAE of 0.81 m. The hindcast obtained by NS_TIDE shows a high consistency with the water level observations at most periods. The correlation coefficient between the model results and the measurements is 0.97. However, the difference between the model results and the measurements is more significant during high-flow events (**Fig. 4b**). As shown in **Fig. 3b**, there is a sudden rise in river discharge in early February 2003 which is caused by flow regulation. This transient high-flow event sharply increases the water levels and depresses the tides at Longview (**Fig. 4a**). The offset between NS_TIDE hindcast and observations (blue dashed box in **Fig. 4a** and **Fig. 4b**) indicates that NS_TIDE successfully reproduces the tidal variations but fails to accurately reconstruct sub-tidal variations during high-flow events.

Fig. 5 displays the time-dependent K_1 and M_2 tidal heights extracted by NS_TIDE. Both K_1 and M_2 tides oscillate following the non-stationary external forcing. The mean amplitudes of the time-dependent K_1 and M_2 tidal constituents at Longview from the NS_TIDE model are 0.19 and 0.45 m, respectively. The amplitudes of the K_1 and M_2 tidal constituents are significantly reduced during the high-flow event in early February 2003 (blue box in **Fig. 5b**). Furthermore, both K_1 and M_2 tides have clear neap-spring oscillations related to semimonthly changing bottom friction.

4.2 The results of EEMD

Water level records at Longview are decomposed into 13 IMFs via EEMD (**Fig. 6**). **Table 3** shows that the mean periods of the most EEMD modes nearly double those of their previous one, indicating that EEMD is a dyadic filter (Wu and Huang, 2004; Flandrin et al., 2004). The mean period and mean amplitude of IMF1 are 4.20 h and 0.04 m, respectively, which indicates that IMF1 mainly consists of high-frequency shallow water constituents. The mean period and mean amplitude of IMF2 are 12.44 h and 0.43 m, respectively, which are nearly the same as the period and amplitude of M_2

tidal constituent (12.42 h and 0.43 m). This indicates that IMF2 is dominated by M_2 tide. The mean period and mean amplitude of IMF3 are 23.57 h and 0.18 m, respectively, very close to the period and amplitude of K_1 tide (23.93 h and 0.20 m), which indicates that IMF3 may be dominated by K_1 tide. For the rest EEMD modes, their mean periods are significantly larger than 1 day. Therefore, they represent sub-tidal oscillations with different time scales. IMF6 (mean period 9.87 days) may correspond to Mt tide (9.12 days) and Mst tide (9.56 days). IMF10 may correspond to the solar annual tide Sa since its mean period is very close to one year. Note that the mean amplitudes IMF11 and IMF12 are nearly zero, while IMF13 is monotonous and does not have any peaks. The sum of IMFs 11-13 may represent the long-term trends that are not resolved in this study because of the length of the data. The sum of IMFs except for the first three can be regarded as sub-tidal water levels (green line in **Fig. 7**). It is obvious that the sub-tidal water levels obtained by EEMD are more accurate than those obtained by NS_TIDE, especially during high-flow events (**Fig. 7**).

To show the mode mixing phenomenon in the EEMD method, spectral analysis is conducted on the IMFs of the EEMD model. It can be seen from **Table 3** that the IMFs from the 4^{th} to the 13^{th} contain the tidal signals with frequency smaller than diurnal tides (D_1), which means those IMFs are from the same tidal species (*i.e.*, subtidal tides, D_0) but with different periods. Therefore, spectral analysis is only applied to the IMF1, IMF2, and IMF3 of the EEMD model to compare their energy distribution with different frequency bands. It can be seen from **Fig. 8a** that Quarter-diurnal (D_4) tides are the strongest in IMF1, but the amplitudes of semi-diurnal (D_2) tides, terdiurnal (D_3), and penta-diurnal (D_5) tides are also noticeable. The IMF2 (**Fig. 8b**) is dominated by D_2 tides, while the amplitudes of D_1, D_3 and D_4 tides are relatively smaller. The IMF 3 (**Fig. 8c**) is dominated by D_1 tides but includes a small part of the energy of D_2 tides. **Fig. 8** indicates that D_2 tides are split into three modes (IMF1, IMF2 and IMF3), while D_1 tides are split into two modes (IMF2 and IMF3). D_3 and D_4 tides are divided into two modes (IMF1 and IMF2). Since these EEMD modes still contain oscillations of dramatically distinct time scales, the problem of mode mixing is not completely solved.

Similarly, spectral analysis is performed on the IMF1 and IMF2 obtained by EMD as they contain the tidal signal with frequencies equal to or higher than diurnal tides. It is clear from **Fig. 9** that IMF1 and IMF2 are dominated by D_2 and D_1 tides, respectively. As displayed in **Fig. 9a**, EMD fails to separate D_3, D_4 and D_5 tides from D_2 tides. Compared to EMD, EEMD (**Fig. 8a** and **Fig. 8b**) partly separates D_3, D_4 and D_5 tides from D_2 tides. However, this separation is not perfect and complete, and thus the problem of mode mixing still exists.

4.3 The results of VMD

The VMD model coefficients of α, τ and ε are specified as 2000, 0, and 10^{-7} which are referred to Dragomiretskiy and Zosso (2014). Water levels at Longview are decomposed into 12 modes through VMD (**Fig. 10**). **Table 4** lists the mean periods and amplitudes of VMD modes. The VMD mode 1 represents the sub-tidal oscillations (mean period 4.74 days). As shown in **Fig. 7**, the sub-tidal water levels obtained by EEMD and VMD are highly consistent with each other. The mean period and mean amplitude of VMD mode 2 are 23.95 h and 0.21 m, respectively, which indicates that mode 2 is dominated by K_1 tide. The mean period and mean amplitude of VMD mode 3 are 12.44 h and 0.45 m, respectively, which indicates that mode 3 is dominated by M_2 tide. For the rest of VMD modes, based on their mean periods and amplitudes, they correspond to D_3, D_4, D_5, D_6, D_7, D_8, D_9, D_{10}, and D_{11} tides, respectively. It should be noted that the mean amplitudes of modes 8-12 are less than 0.01 m, which means that they are relatively insignificant to the total water level variations.

Fig. 11 shows the Fourier spectrum maps of modes 2-9 obtained by VMD to compare the energy distribution of the modes with frequencies between D_1 to D_8 tides. Mode 2 only contains D_1 tides, while mode 3 only contains D_2 tides. Modes 4-9 only have D_3 – D_8 tides, respectively. Comparing **Fig. 11** to **Fig. 8**, it is clear that the oscillations with different time scales are strictly divided into different VMD modes and no mode mixing exists. All tidal species are perfectly separated from each other, which can be illustrated by **Eq. (13)**. The center frequencies of each VMD mode are respectively estimated based on the center-of-gravity of each mode's power spectrum and they will be allocated to different tidal species. Estimating each VMD mode through the frequency domain enables the VMD method to be less sensitive to noises and have the advantage of avoiding mode mixing.

The upper envelope of mode 3 and mode 4 in **Fig. 10** can be regarded as D_2 and

D_3 amplitudes, respectively (**Fig. 12**). Both D_2 and D_3 amplitudes show clear semimonthly cycles related to neap-spring variations in bottom friction. These semimonthly cycles in tidal amplitudes are larger when the river discharge decreases, which is consistent with the theory of **Eq. (4)** and **Eq. (5)**. D_2 amplitude is negatively correlated to the river discharge. For example, when the total river discharge of Columbia River and Willamette River peaked in early February 2003 (**Fig. 12b**), the D_2 amplitude reached the minimum at the same time (blue dashed line in **Fig. 12a**). However, **Fig. 12c** shows that the D_3 amplitude did not reach the lowest value when the river discharge peaked in early February 2003. This indicates that the response of D_3 tides to river discharge is distinct from D_2 tides. D_2 tides are astronomical, while D_3 tides are nearly non-astronomical and mainly generated from the nonlinear interaction between D_1 and D_2 tides. For example, the largest tidal constituent in D_3 tides at Longview is MK_3 which is originated from the nonlinear interaction between K_1 and M_2 tides. For these shallow water tidal constituents, the effect of river discharge is dual. First, river discharge enhances the nonlinear interaction between major tides and transfers the energy from D_1 and D_2 tides to shallow water constituents. Second, river discharge plays a frictional effect on tides and thereby impedes the propagation of tides. The increment of river discharge can enhance the energy transfer from D_1 and D_2 tides to D_3 tides but also play a stronger frictional effect on D_3 tides. The dual effects of river discharge on tides are also reported in previous studies (Guo et al., 2015; Guo et al., 2020). Therefore, the response curve of D_3 amplitudes to river discharge should be nonmonotonic and may exist a threshold value. In general, the VMD method captured the non-stationary feature of tides successfully.

5. Discussions

5.1 Detiding river discharge data

In section 4, the performance of VMD on processing estuarine water levels is shown. In fact, in tidal rivers, not only water levels but also river discharge observations are modulated by tides. Such tidal modulations are complicated and present strong non-stationarity. Removing the non-stationary tidal influence from observations is usually called as "detiding" (Hoitink and Jay, 2016). Detiding is a general challenge but a fundamental task. Accurate removal of tidal discharge from observed discharge time series is necessary and vital for numerous proposes, such as climate analyses, freshwater resources management, and coastal ecosystem research (Moftakhari et al., 2013, 2016).

Fig. 13a displays the observed hourly river discharge (provided by USGS) for a year (October 2007 - October 2008) at Portland, Oregon (**Fig. 2**). Positive discharge values mean that flow propagates seaward, while negative discharge values mean that flow propagates landward. It can be seen from **Fig. 13a** that the flow direction of the observed discharge changes with time. When freshwater discharge is large, tidal discharge is negligible. However, when freshwater discharge becomes weak, tidal discharge becomes significant. To obtain freshwater discharge, the VMD method is used on the river discharge measurements (**Fig. 13a**). **Fig. 13b** shows the freshwater discharge extracted by VMD (red line). VMD accurately removes the non-stationary tidal discharge and obtains reliable freshwater discharge. The Fourier spectrum maps of the related VMD modes 2-9 are displayed in **Fig. 14**. The D_1 to D_8 tides are perfectly divided into different VMD modes, while the energy from freshwater discharge is fully extracted out.

The same detiding works are conducted again by EEMD for further comparison. The Fourier spectrum maps of EEMD IMFs 1-4 are displayed in **Fig. 15**. The D_4 tide energy appears in IMF1 and IMF2, while D_2 tide energy resides in IMF2 and IMF3. The D_1 tides majorly exist in IMF4 but partly arises in IMF2. **Fig. 15** clearly shows that the mode mixing phenomenon also exists when the EEMD method is used to decompose the time series of river discharge influenced by tides. Compared to EEMD, it is clear from **Fig. 14** that VMD is more suitable to remove tidal discharge and analyze the multi-time scale tidal variability in discharge time series.

5.2 Advantages and Disadvantages of NS_TIDE, EEMD and VMD

Compared to NS_TIDE which is specially designed for water levels in tidal rivers, both EEMD and VMD are general methods for all kinds of non-stationary and nonlinear time series. In section 5.1, the application of the VMD method to separate freshwater discharge from observed river discharge containing tidal discharge is demonstrated. In fact, not only discharge, water temperature, turbidity, suspended sediment concentration and other parameters in fluvial estuaries are all influenced by tide-river interaction. These parameters can also be analyzed by VMD. In this paper, river tides are used as an instance to illustrate the application of VMD. However, it is fully expected that VMD is also suitable for other non-stationary tides, while NS_TIDE is not suitable. Furthermore, by comparing the results of VMD and NS_TIDE, this study points out again that NS_TIDE cannot accurately reproduce sub-tidal water levels during high-flow events. Gan et al. (2019) proposed a modified NS_TIDE model which replaced the stage model with the frequency-expanded tidal-fluvial model. Although the hindcast of the modified NS_TIDE has been obviously improved compared to the original NS_TIDE model, the accuracy of the predicted water levels obtained by the modified NS_TIDE is virtually reduced due to overfitting.

Compared to EMD, although the results of EEMD are improved and the problem of mode mixing is partly solved to some extent, there is still room for further improvement. In comparison with EEMD, VMD perfectly eliminates mode mixing and each mode only contains oscillations with similar frequencies. When applied to estuarine tide levels, each VMD mode has a physical meaning and is related to tidal species. The non-stationary features captured by the VMD model are generally consistent with the theory of tide-river interplay.

Although powerful and useful, VMD also has potential limitations. VMD can only separate different tidal species from each other and cannot extract specific tidal constituents such as the M_2, S_2, K_1 and O_1 tidal constituents. This is actually the common limitations of signal analysis tools because they need to make a tradeoff between the resolutions in time domain and frequency domain. All signal analysis methods follow the Heisenberg Principle (Flinchem and Jay, 2000). With the increase of the resolution in the time domain, their resolution in the frequency domain should decline. M_2 and S_2 tidal constituents belong to D_2 tides due to their close frequency. They are divided into the same VMD mode (Mode 3 in **Fig. 10**). However, they can not be further separated because of the resolution limitation of the VMD model in the frequency domain. Relative to the signal analysis methods such as the VMD and EEMD models, NS_TIDE may be the only tool to extract specific tidal constituents but also keep the time-dependent tide properties. In other words, the NS_TIDE model has the finest resolution in the frequency domain.

6. Conclusions

The VMD method has been widely used to analyze various signals, but to our knowledge, the application of VMD to non-stationary tides is nonexistent. Application of the VMD method to analyze river tides is a new idea that is verified in this research for the first time. VMD strictly divides different tidal species into different modes, and thus avoids mode mixing. The non-stationary characteristics of tides induced by tide-river interaction are captured accurately. The sub-tidal water levels obtained by VMD are highly consistent with those obtained by EEMD and more accurate than those obtained by NS_TIDE. As the first effort to adopt the VMD method to separate tidal discharge from freshwater discharge, it is found in this study that VMD is superior to

EEMD when dealing with non-stationary tidal time series.

Both VMD and NS_TIDE are useful non-stationary signal analysis tools. The biggest advantage of NS_TIDE over the VMD method is the capacity to resolve specific tidal constituents. Compared to NS_TIDE, a great advantage of the VMD is that it is a general method and can be applied to analyze non-stationary tidal time series with dynamic mechanisms unclear. The combination of VMD and NS_TIDE can help us know more about water level dynamics in tidal rivers, and thus better protecting people who live nearby the river. It is expected that the VMD method can prove its value in future studies of the non-stationary and nonlinear processes like internal tides or tidal influence on the environment.

Acknowledgements

Tide data were provided by the National Oceanic and Atmospheric Administration (https://tidesandcurrents.noaa.gov). Flow data were provided by the U.S. Geological Survey (https://nwis.waterdata.usgs.gov/nwis). The authors thank Pascal Matte for providing the NS_TIDE package and partly of the observations. The authors thank Rich Pawlowicz for distributing the T_TIDE package. The authors thank Zhaohua Wu for distributing the EEMD package. The authors also appreciate Dominique Zosso for providing the VMD toolbox which can be downloaded from the following website: https://ww2.mathworks.cn/matlabcentral/fileexchange/44765-variational-mode-decomposition?s_tid=srchtitle. This work was partly supported by the National Natural

Science Foundation of China [Grant No: 51979076], and the Fundamental Research Funds for the Central Universities of China [Grant Nos: B200204017; 2018B635X14] and the Postgraduate Research & Practice Innovation Program of Jiangsu Province [Grant No: KYCX18_0602]. The first author also would like to acknowledge the financial support from the China Scholarship Council (CSC) under the PhD exchange program [201906710022] with Cardiff University.

Data Availability Statement: All the data used in this study are available by contacting the corresponding author.

Reference

Amin, M., 1982: On analysis and prediction of tides on the west coast of Great Britain. *Geophys. J. Int.*, **68**, 57–78, doi:10.1111/j.1365-246X.1982.tb06962.x.

Cai, H., Q. Yang, Z. Zhang, X. Guo, F. Liu, and S. Ou, 2018: Impact of River-Tide Dynamics on the Temporal-Spatial Distribution of Residual Water Level in the Pearl River Channel Networks, *Estuaries and Coasts*, **41**, 1885-1903, doi:10.1007/s12237-018-0399-2.

Chen, Y., M. Gan, S. Pan, H. Pan, X. Zhu, and Z. Tao, 2020: Application of auto-regressive (AR) analysis to improve short-term prediction of water levels in the Yangtze estuary, *J. Hydrol.*, **590**,125386.

Cheng, Y., T. Ezer, and B. Hamlington, 2016: Sea Level Acceleration in the China Seas.

Water, **8**, 293, doi:10.3390/w8070293.

Cheng, Y., T. Ezer, L. P. Atkinson, and Q. Xu, 2017: Analysis of tidal amplitude changes using the EMD method. *Cont. Shelf Res.*, **148**, 44–52, doi:10.1016/j.csr.2017.09.009.

Devlin, A. T., Pan, J., and Lin, H., 2020: Multi-timescale analysis of tidal variability in the Indian Ocean using Ensemble Empirical Mode Decomposition. *Journal of Geophysical Research:Oceans*, 125(12), e2020JC016604.

Dragomiretskiy, K. and D. Zosso, 2014: Variational Mode Decomposition, *IEEE Trans. Signal Processing*, **62**, 531-544.

Ezer, T., 2013: Sea level rise, spatially uneven and temporally unsteady: Why the U.S. East Coast, the global tide gauge record, and the global altimeter data show different trends. *Geophys. Res. Lett.*, **40**, 5439–5444, doi:10.1002/2013GL057952.

Ezer, T., I. D. Haigh, and P. L. Woodworth, 2016: Nonlinear sea-level trends and long-term variability on Western European Coasts. *J. Coast. Res.*, **320**, 744–755, doi:10.2112/JCOASTRES-D-15-00165.1.

Ezer, T., 2019: Regional differences in sea level rise between the Mid-Atlantic Bight and the South Atlantic Bight: Is the gulf stream to blame?. Earth's Future, 7, 771–783, doi:10.1029/2019EF001174.

Flandrin, P., G. Rilling, and P. Goncalves, 2004: Empirical mode decomposition as a filter bank. *IEEE Signal Process. Lett.*, **11**, 112–114, doi:10.1109/LSP.2003.821662.

Flinchem, E.P. and Jay, D.A., 2000: An introduction to wavelet transform tidal analysis methods. *Estuarine, Coastal and Shelf Science*, 51(2), 177-200, doi:10.1006/ecss.2000.0586.

Foreman, M. G. G., and R. F. Henry, 1989: The harmonic analysis of tidal model time series. *Adv. Water Resour.*, **12**, 109–120, doi:10.1016/0309-1708(89)90017-1.

Gan, M., Pan, S., Chen, Y., Cheng, C., Pan, H., and Zhu, X., 2021: Application of the machine learning LightGBM model to the prediction of the water levels of the lower Columbia River. *Journal of Marine Science and Engineering*, **9**, 496, doi: 10.3390/jmse9050496.

Gan, M., Y. Chen, S. Pan, J. Li, and Z. Zhou, 2019: A modified nonstationary tidal harmonic analysis model for the Yangtze Estuarine tides. *J. Atmos. Oceanic Technol.,* **36(4)**, 513–525, doi: 10.1175/JTECH-D-18-0199.1.

Guo, L.C., Mick, V. D. W., Jay, D.A., Matte, P, Wang, Z.B., Roelvink, D., and He, Q., 2015: River-tide dynamics: Exploration of nonstationary and nonlinear tidal behavior in the Yangtze River estuary. *J. Geophys. Res. Oceans*, **120**, 3499-3521, doi:10.1002/2014JC010491.

Guo, L., Wang, Z. B., Townend, I., and He, Q., 2019: Quantification of tidal asymmetry and its nonstationary variations. *Journal of Geophysical Research: Oceans*, **124**, doi:10.1029/2018JC014372.

Hoitink, A. J. F., and D. A. Jay, 2016: Tidal river dynamics: Implications for deltas. *Rev. Geophys.*, **54**, 240–272, doi:10.1002/2015RG000507.

Huang, N. E., Z. Shen, S. R. Long, M. C. Wu, H. H. Shih, N. Yen, C. C. Tung, and H. H. Liu, 1998: The empirical mode decomposition and the Hilbert spectrum for nonlinear and non-stationary time series analysis. *R. Soc. Publ.*, **454**, 903–995, doi:10.1098/rspa.1998.0193.

Jalón-Rojas, I., Sottolichio, A., Hanquiez, V., Fort, A., and Schmidt, S., 2018: To what extent multidecadal changes in morphology and fluvial discharge impact tide in a convergent (turbid) tidal river. *J. Geophys. Res. Oceans*, *123(5)*, 3241-3258, doi:10.1002/2017JC013466.

Jay, D.A. and Kukulka, T., 2003: Revising the paradigm of tidal analysis? The uses of non-stationary data. *Ocean Dynamics*, **53(3)**, 110-125, doi: 10.1007/s10236-003-0042-y.

Jay, D. A., and E. P. Flinchem, 1997: Interaction of fluctuating river flow with a barotropic tide: A demonstration of wavelet tidal analysis methods. *J. Geophys. Res*., **102 (C3)**, 5705–5720.

Jay, D. A., and E. P. Flinchem, 1999: A comparison of methods for analysis of tidal records containing multi-scale non-tidal background energy. *Cont. Shelf Res.*, **19**, 1695–1732.

Jay, D. A., K. Leffler, and S. Degens, 2011: Long-term evolution of Columbia River tides. *J. Waterw. Port Coastal Ocean Eng*., **137**, 182–191, doi: 10.1007/s12237-014-9819-0.

Jay, D. A., K. Leffler, H. L. Diefenderfer, and A. B. Borde, 2014: Tidal-fluvial and estuarine processes in the Lower Columbia River: I. Along-channel water level variations, Pacific Ocean to Bonneville Dam. *Estuaries and Coasts*, **38**, 415–433, doi:10.1007/s12237-014-9819-0.

Ji, F., Z. Wu, J. Huang, and E. P. Chassignet, 2014: Evolution of land surface air temperature trend. *Nat. Clim. Chang.*, **4**, 462–466, doi:10.1038/nclimate2223.

Kukulka, T., and D. A. Jay, 2003: Impacts of Columbia River discharge on salmonid habitat: 1. A nonstationary fluvial tide model. *J. Geophys. Res. Ocean.*, **108**, 3293, doi:10.1029/2002JC001382.

Kukulka, T., and D. A. Jay, 2003b: Impacts of Columbia River discharge on salmonid habitat: 2. Changes in shallow-water habitat. *J. Geophys. Res. Ocean* , **108**, 3294, doi:10.1029/2003JC001829.

Leffler, K. E., and D. A. Jay, 2009: Enhancing tidal harmonic analysis: Robust (hybrid L1/L2) solutions. *Cont. Shelf Res.*, **29**, 78–88.

Matte, P., D. A. Jay, and E. D. Zaron, 2013: Adaptation of classical tidal harmonic analysis to nonstationary tides, with application to river tides. *J. Atmos. Ocean. Technol.*, **30**, 569–589, doi:10.1175/JTECH-D-12-00016.1.

Matte, P., Y. Secretan, and J. Morin, 2014: Temporal and spatial variability of tidal-fluvial dynamics in the St. Lawrence fluvial estuary: An application of nonstationary tidal harmonic analysis, *J. Geophys. Res. Oceans*, **119**, 5724–5744, doi:10.1002/2014JC009791.

Matte, P., Y. Secretan, and J. Morin (2018), Reconstruction of tidal discharges in the St.

Lawrence Fluvial Estuary: The method of cubature revisited, *J. Geophys. Res. Ocean.*, *123*(8), 5500–5524, doi:10.1029/2018JC013834.

Matte, P., Y. Secretan, and J. Morin (2019), Drivers of residual and tidal flow variability in the St . Lawrence Fluvial Estuary : Influence on tidal wave propagation, *Cont. Shelf Res.*, *174*(February 2019), 158–173, doi:10.1016/j.csr.2018.12.008.

Moftakhari, H. R., D. A. Jay, S. A. Talke, T. Kukulka, and P. D. Bromirski, 2013: A novel approach to flow estimation in tidal rivers. *Water Resour. Res.*, **49**, 4817–4832, doi:10.1002/wrcr.20363.

Moftakhari, H. R., D. A. Jay, and S. A. Talke, 2016: Estimating river discharge using multiple-tide gauges distributed along a channel. *J. Geophys. Res. Ocean.*, **121**, 2078–2097, doi:10.1002/2015JC010983.

Naik, P. K., and D. A. Jay, 2011: Human and climate impacts on Columbia River hydrology and salmonids. *River Res. Appl.*, **27**, 1270–1276, doi:10.1002/rra.1422.

Ni, P., Li, J., Hao, H., Xia, Y., Wang, X., Lee, J.M., Jung, K.H., 2018: Time-varying system identification using variational mode decomposition. Structural Control and Health Monitoring, e2175, doi: 10.1002/stc.2175.

Nidzieko, N.J., 2010: Tidal asymmetry in estuaries with mixed semidiurnal/diurnal tides. *J. Geophys. Res.*, 115(C8), doi:10.1029/2009JC005864.

Pan, H., Z. Guo, and X. Lv, 2017: Inversion of tidal open boundary conditions of the m2 constituent in the Bohai and Yellow Seas. *J. Atmos. Ocean. Technol.*, **34**, 1661-1672, doi:10.1175/JTECH-D-16-0238.1.

Pan, H., Z. Guo, Y. Wang, and X. Lv, 2018a: Application of the EMD method to river tides. *J. Atmos. Ocean. Technol.*, **35**, 809–819, doi:10.1175/JTECH-D-17-0185.1.

Pan, H., X. Lv, Y. Wang, P. Matte, H. Chen, and G. Jin, 2018b: Exploration of tidal-fluvial interaction in the Columbia River Estuary using S_TIDE. *J. Geophys. Res. Ocean.*, 1–22, doi:10.1029/2018JC014146.

Pan, H., and X. Lv, 2019: Reconstruction of spatially continuous water levels in the Columbia River Estuary: The method of Empirical Orthogonal Function revisited, *Estuar. Coast. Shelf Sci.*, 222(April), 81–90.

Pawlowicz, R., B. Beardsley, and S. Lentz, 2002: Classical tidal harmonic analysis including error estimates in MATLAB using T_TIDE. *Comput. Geosci*., **28**, 929–937.

Wu, Z., and N. E. Huang, 2004: A study of the characteristics of white noise using the empirical mode decomposition method. *Proc. R. Soc. A Math. Phys. Eng. Sci.*, **460**, 1597–1611, doi:10.1098/rspa.2003.1221.

Wu, Z., and N. E. Huang, 2009: Ensemble empirical mode decomposition: a noise-assisted data analysis method, *Advances in adaptive data analysis*, **1**, 1-41, doi:10.1142/S1793536909000047.

Wu, Z., E. K. Schneider, B. P. Kirtman, E. S. Sarachik, N. E. Huang, and C. J. Tucker, 2008: The modulated annual cycle: An alternative reference frame for climate anomalies. *Clim. Dyn.*, **31**, 823–841, doi:10.1007/s00382-008-0437-z.

Zhang, J., Yan, R., Gao, R.X., Feng, Z., 2010: Performance enhancement of ensemble empirical mode decomposition. *Mechanical Systems and Signal Processing*, 24, 2104-2123, doi:10.1016/j.ymssp.2010.03.003.

Zhang, W., Y. Cao, Y. Zhu, J. Zheng, X. Ji, Y. Xu, Y. Wu, and A. J. F. Hoitink, 2018: Unravelling the causes of tidal asymmetry in deltas. *J. Hydrol.*, **564**, 588–604, doi:10.1016/j.jhydrol.2018.07.023.

Zosso, D., 2021: Variational Mode Decomposition (https://www.mathworks.com/matlabcentral/fileexchange/44765-variational-mode-decomposition), MATLAB Central File Exchange. Retrieved February 22, 2021.

Tables:

Table 1. Tidal constituents at Longview (rkm 107) with amplitudes greater than 0.05 m and signal-to-noise ratios (SNRs) greater than two (extracted from the data of 2003 by the CHA method).

Tidal Constituent	Amplitude (m)	Phase (deg)	Signal-to-noise ratio (SNR)
Sa	0.38	257.22	21
Ssa	0.13	302.57	3.3
Msf	0.17	312.29	5.7
O_1	0.10	347.25	410
P_1	0.05	274.76	160
K_1	0.20	265.75	1800
N_2	0.08	225.39	98
M_2	0.43	331.31	3200
S_2	0.10	284.68	150
K_2	0.05	86.67	44
MO_3	0.05	231.23	80
MK_3	0.07	156.76	89
M_4	0.08	230.00	300

Table 2. Selected 26 tidal constituents in the NS_TIDE model for the water levels at Longview in 2003.

Tidal species	Tidal constituents
D_1	ALP_1, SIG_1, Q_1, O_1, NO_1, K_1, J_1, SO_1, UPS_1
D_2	EPS_2, N_2, M_2, S_2
D_3	MO_3, MK_3, SK_3
D_4	MN_4, M_4, MS_4, SK_4
D_5	$2MK_5$
D_6	$2MN_6$, M_6, $2MS_6$
D_7	$3MK_7$
D_8	M_8

Table 3. Mean amplitudes and periods of EEMD modes at Longview station for the water levels of 2003

Mode	Number of peaks	Mean period (day)	Mean amplitude (m)
1	2089	0.18	0.04
2	705	0.52	0.43
3	372	0.98	0.18
4	223	1.64	0.03
5	89	4.10	0.05
6	37	9.87	0.11
7	20	18.26	0.08
8	8	45.66	0.13
9	4	91.32	0.08
10	1	365.30	0.23
11	1	365.30	0.00
12	1	365.30	0.00
13	-	-	-

Table 4. Mean amplitudes and periods of VMD modes at Longview station for the water levels of 2003

Mode	Number of peaks	Mean period (day)	Mean amplitude (m)
1	77	4.74	1.69
2	366	1.00	0.21
3	705	0.52	0.45
4	1072	0.34	0.09
5	1411	0.26	0.10
6	1762	0.21	0.03
7	2122	0.17	0.01
8	2479	0.15	0.008
9	2830	0.13	0.007
10	3194	0.11	0.005
11	3622	0.10	0.002
12	4142	0.09	0.002

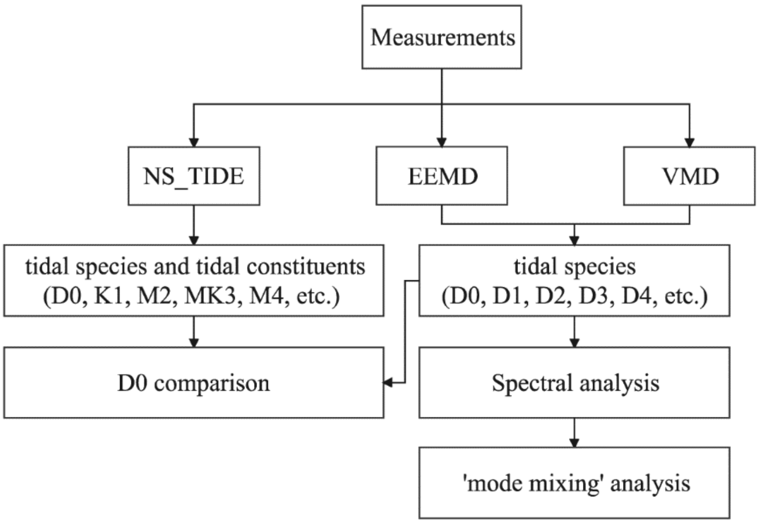

Fig. 1. Flowchart of this study.

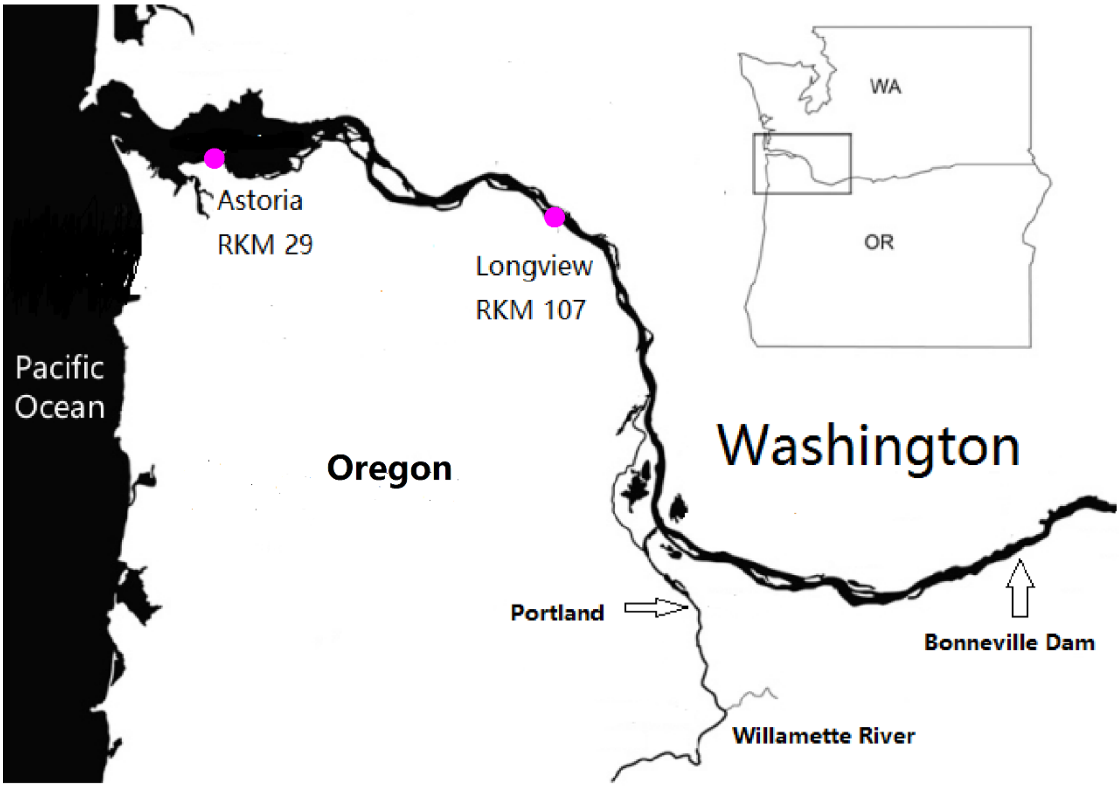

Fig. 2. Map of the Columbia River Estuary and the location of the tide gauges.

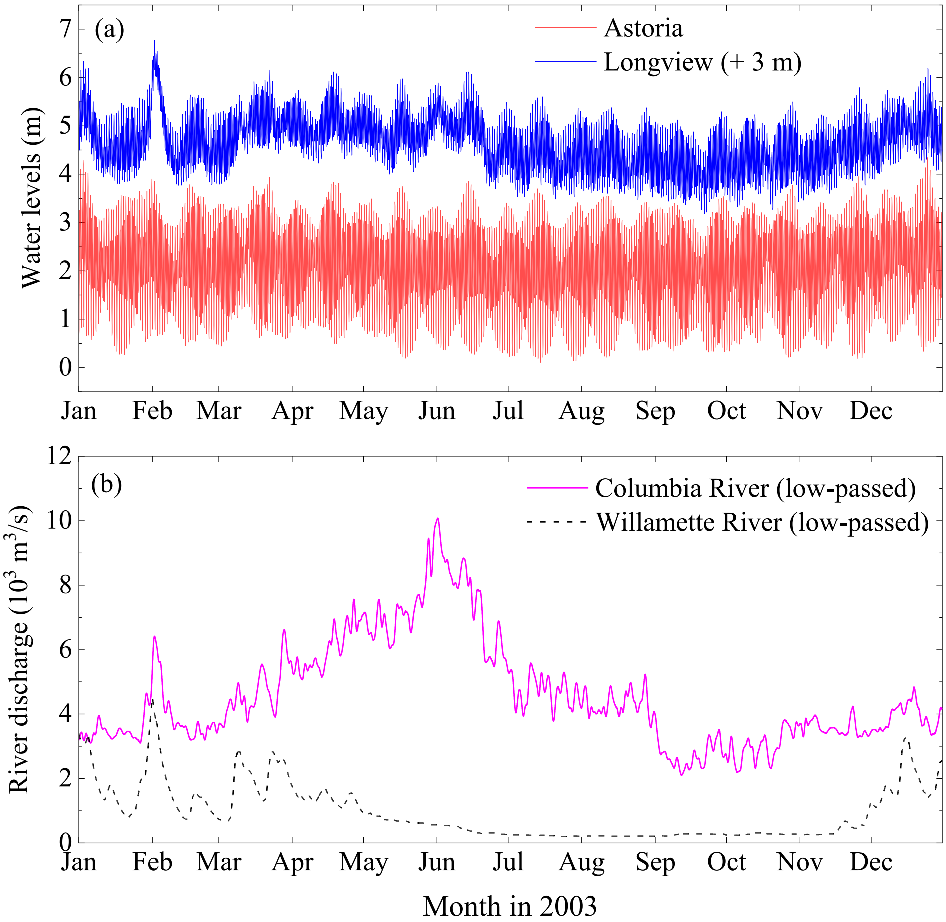

Fig. 3. (a) Water level observations at Astoria and Longview (increased by 3 m) in 2003. (b) Synchronous river discharge for the Willamette River and the main stem of the Columbia River (at Bonneville Dam).

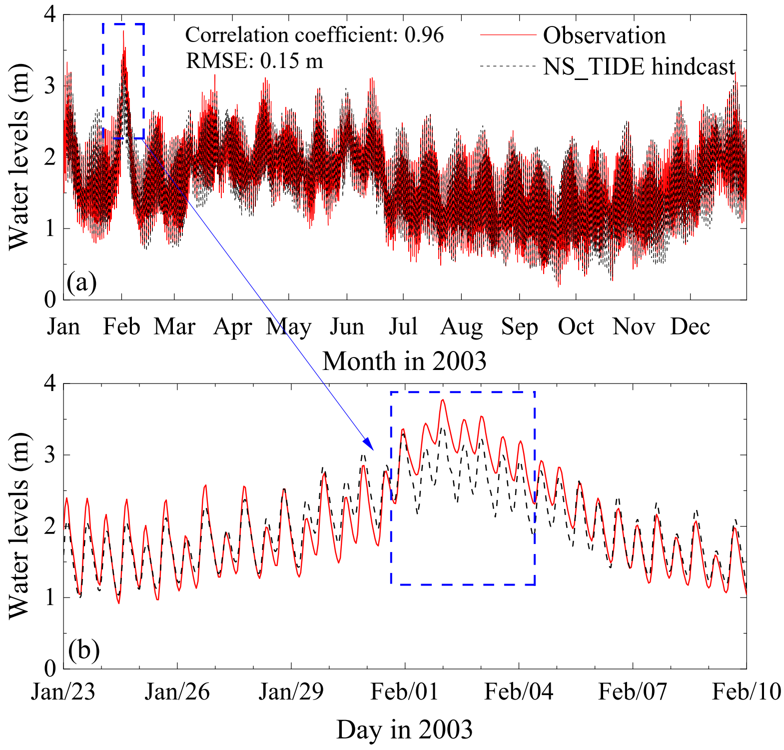

Fig. 4. (a) Water level observations in 2003 of Longview station and the synchronous hindcast results of the NS_TIDE model. (b) Same as (a), but in early February 2003.

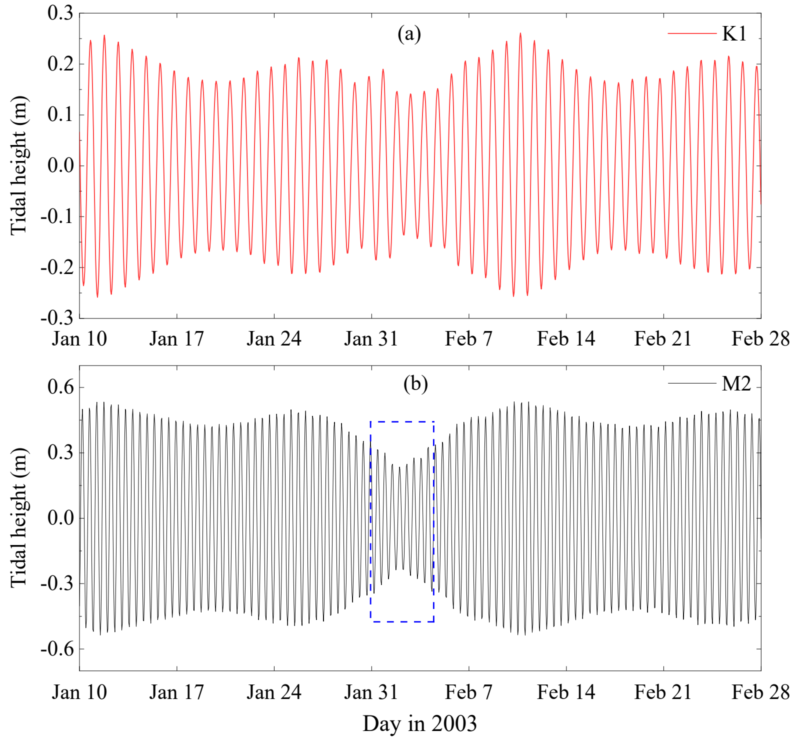

Fig. 5. Extracted time-dependent K_1 (a) and M_2 (b) tidal heights between January 10 to February 28 of 2003 from the NS_TIDE model hindcast results of Longview station.

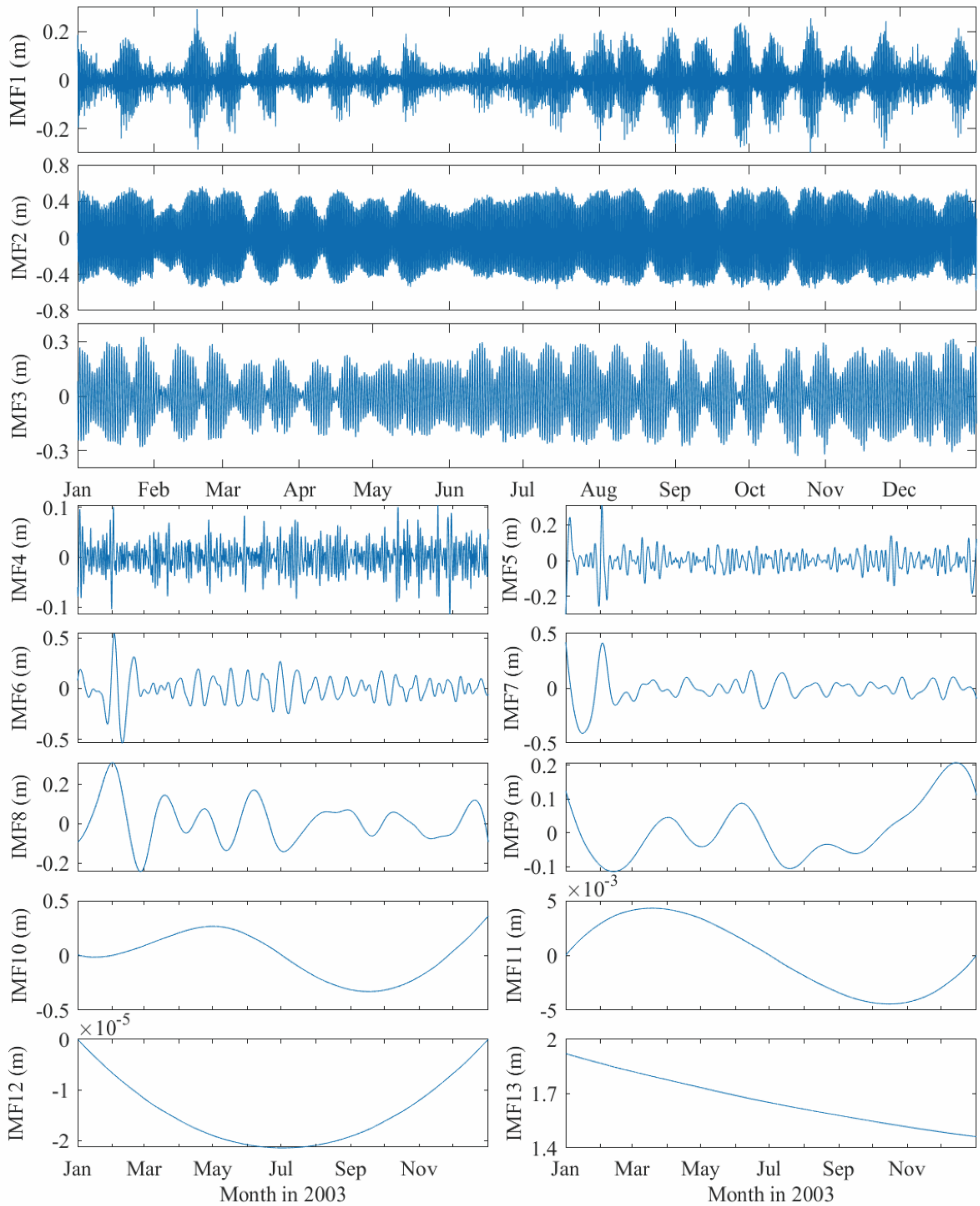

565

566 Fig. 6. The EEMD modes for the water levels of Longview station in 2003.

567

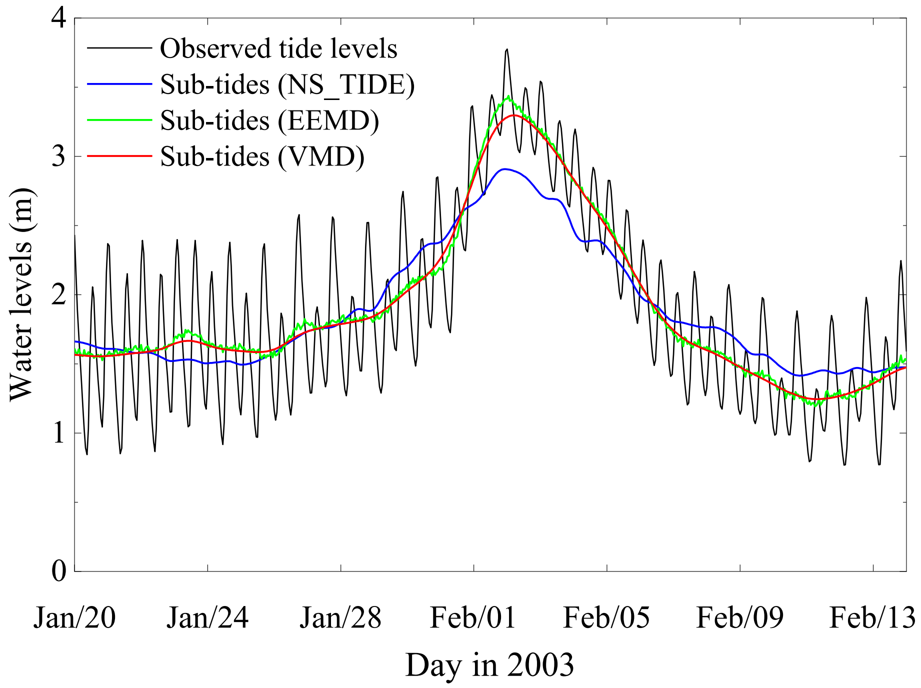

Fig. 7. Comparison of the sub-tidal water levels between January 20 and February 13 of 2003 obtained by the NS_TIDE, EEMD, and VMD models.

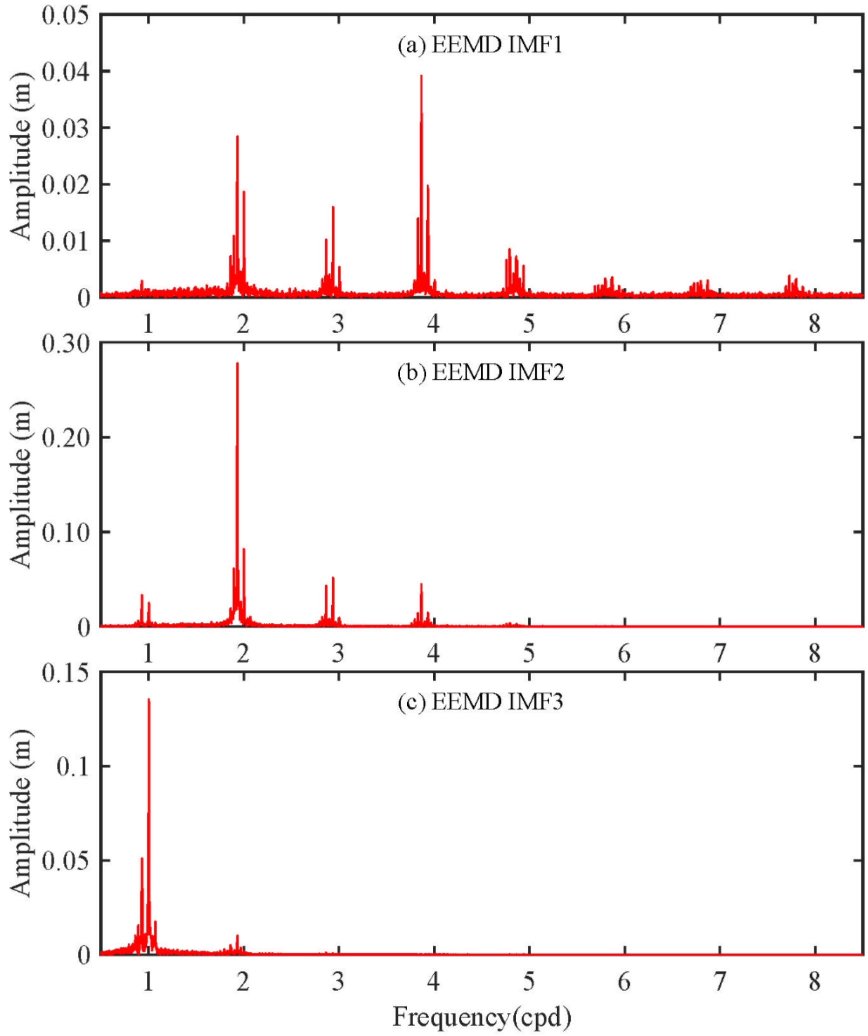

Fig. 8. Fourier spectra map for (a) EEMD IMF 1, (b) IMF 2, and (c) IMF 3 for the water levels of Longview station in 2003.

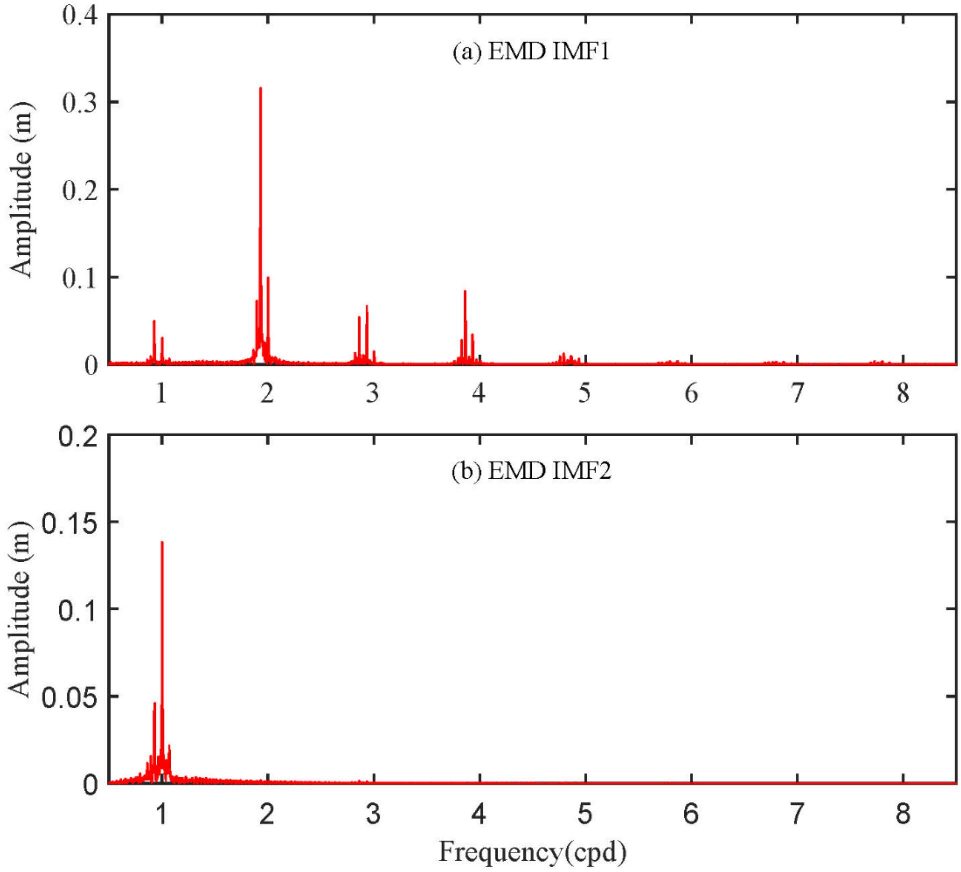

Fig. 9. Fourier spectra map for (a) EMD mode 1 (b) mode 2 for the water levels of Longview station in 2003.

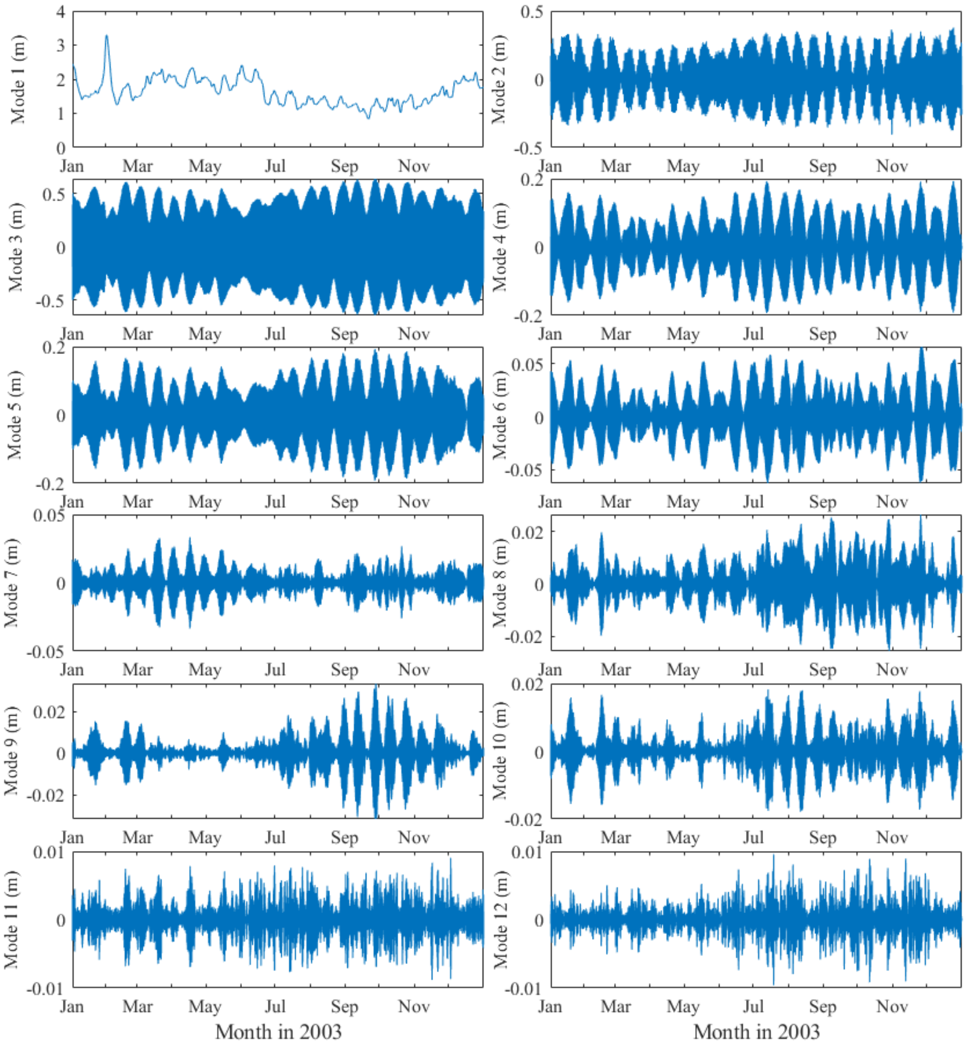

Fig. 10. The 12 VMD modes for the water levels of Longview station in 2003.

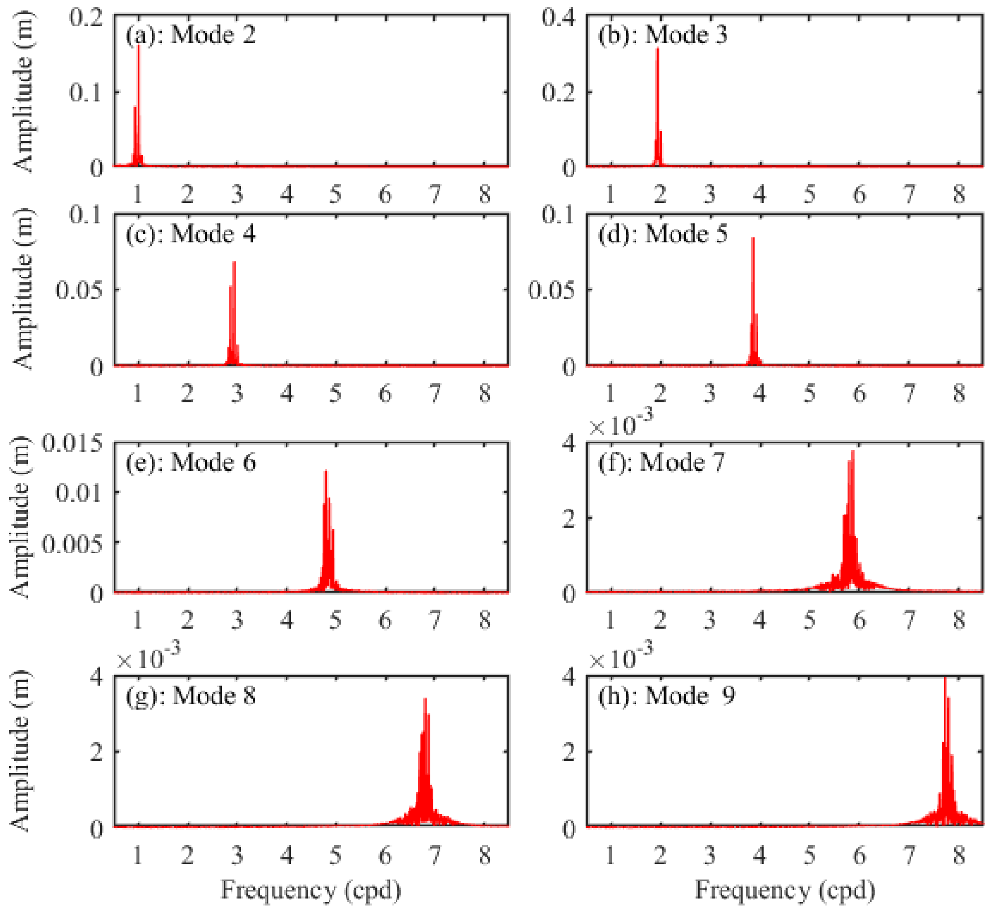

Fig. 11. Fourier spectra map of the VMD model from mode 2 to mode 9 for the water levels of Longview station in 2003.

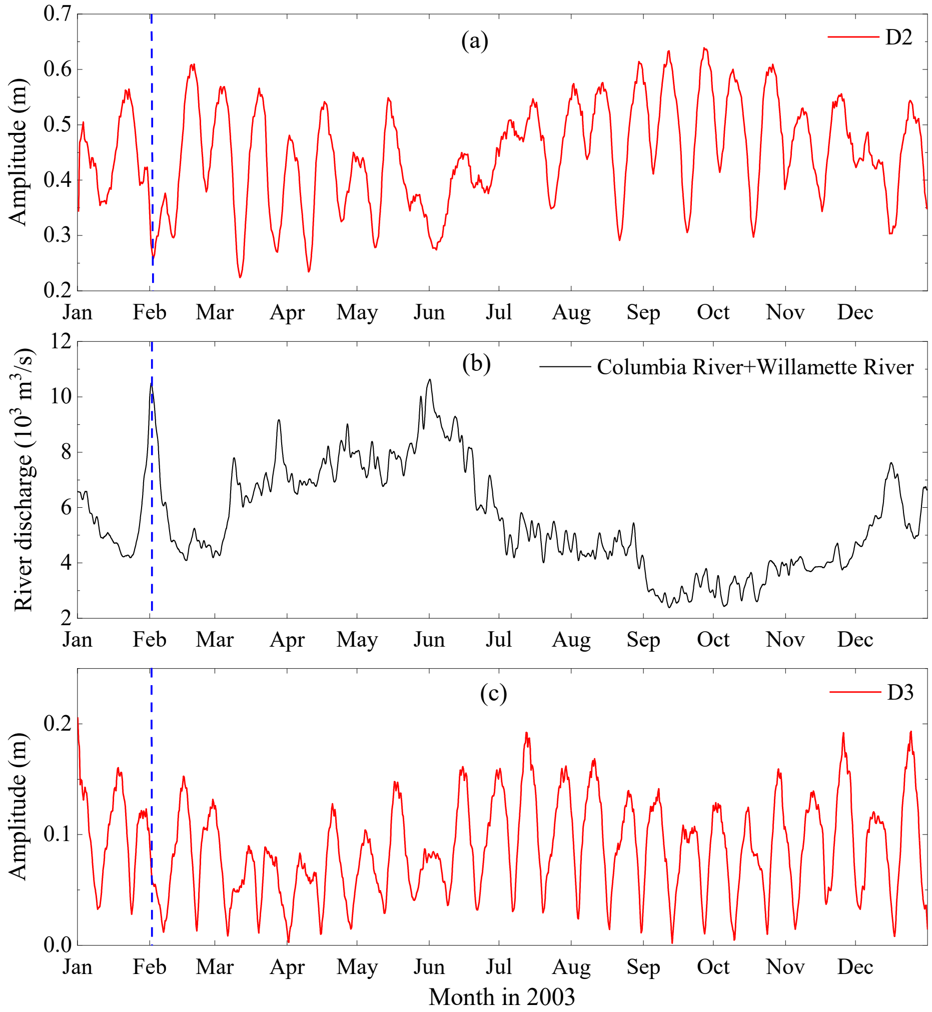

Fig. 12. (a) D2 amplitudes at Longview (b) Discharge forcing in the lower Columbia River (sum of river discharge at Bonneville Dam of Columbia River and Portland of Willamette River); (c) D3 amplitudes at Longview for the data in 2003.

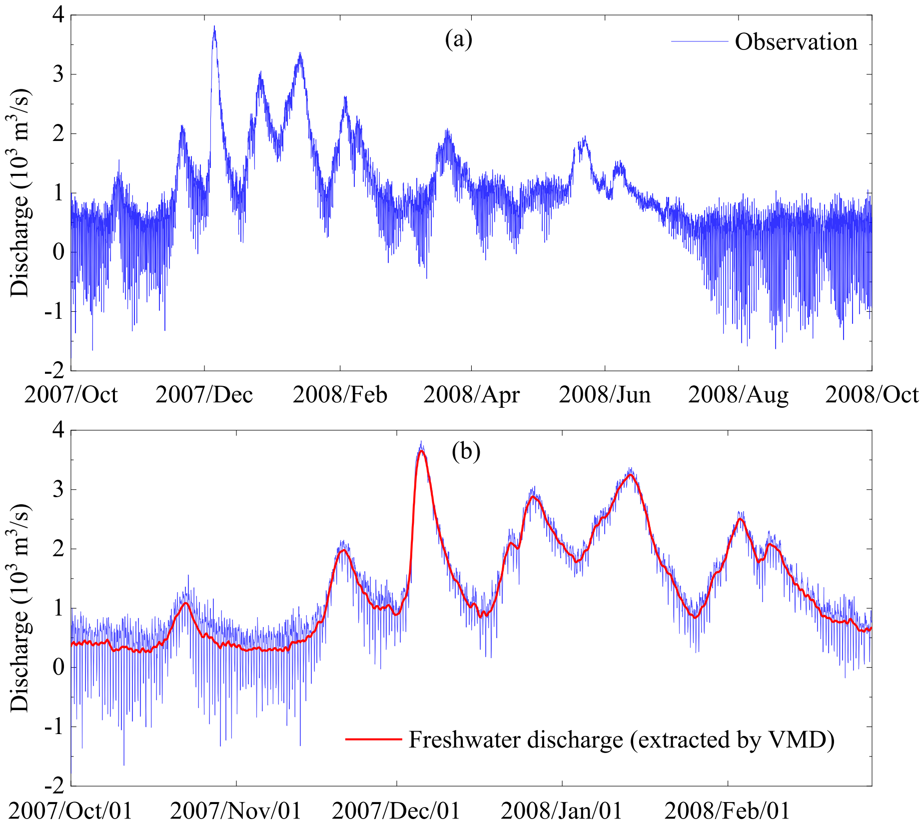

Fig. 13. (a) Portland discharge observations from 2007 October to 2008 October. (b) Freshwater discharge obtained by VMD from October 2007 to February 2008.

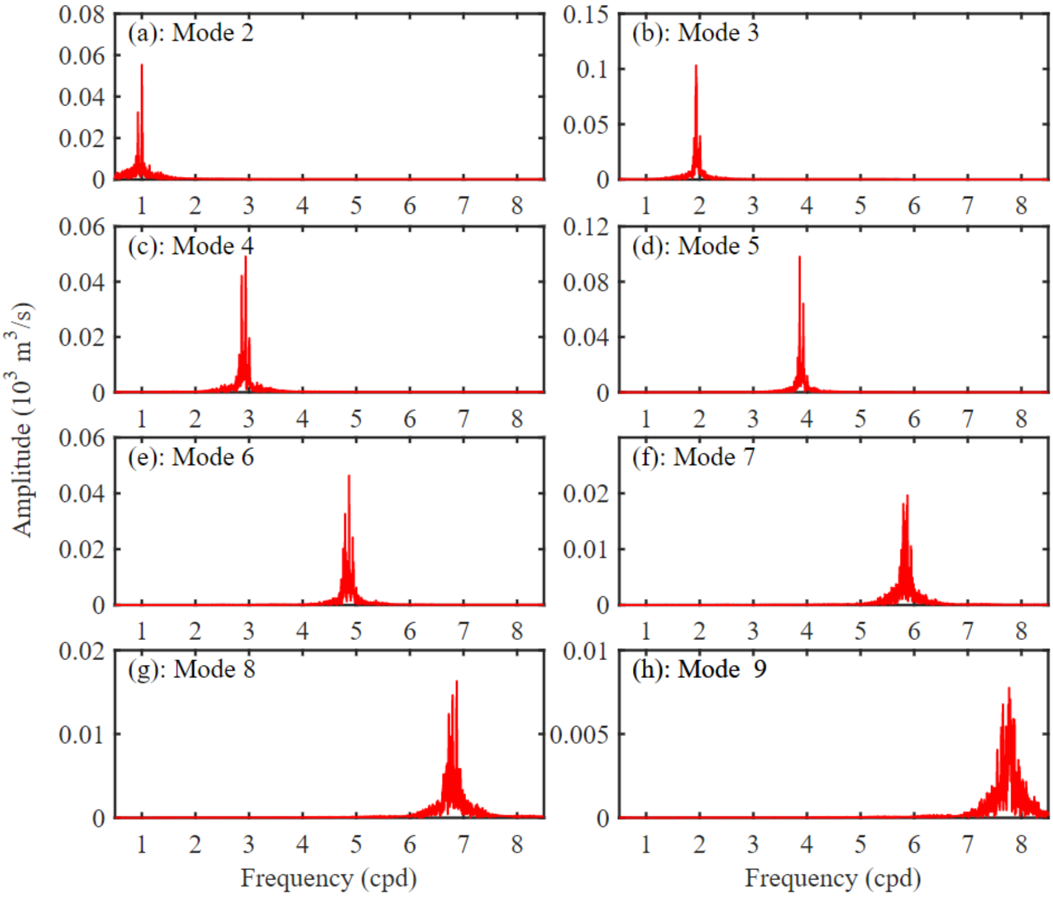

Fig. 14. Fourier spectra map of the VMD model from mode 2 to mode 9 for the observed river discharge of Portland station between 2007 October and 2008 October.

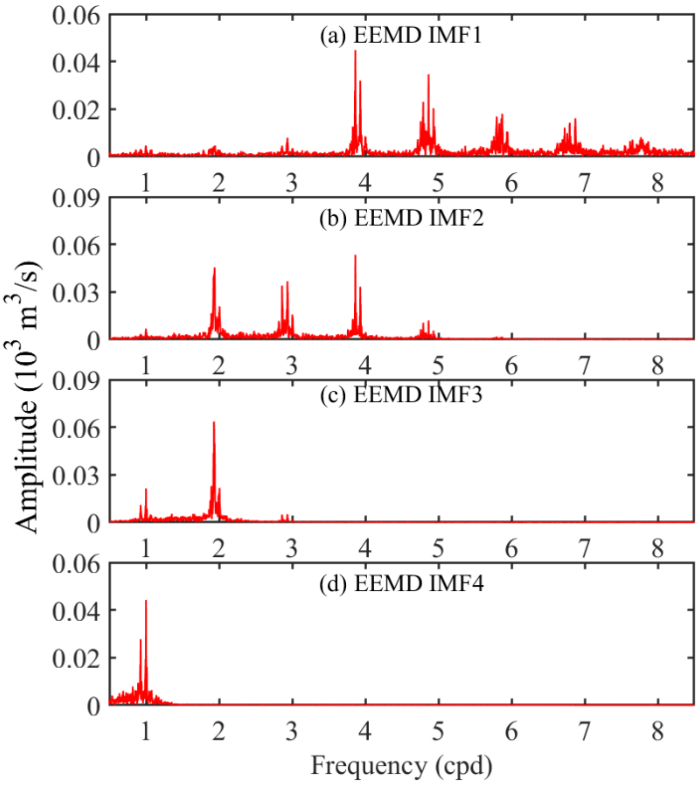

Fig. 15. Fourier spectra map of the EEMD model from IMF 1 to IMF 4 for the observed river discharge of Portland station between 2007 October and 2008 October.